Histotripsy Cardiac Therapy System Integrated with Real-time Motion Correction

Ryan M. Miller[1], **Yohan Kim**[1], **Kuang-Wei Lin**[1], **Charles A. Cain**[1], **Gabe E. Owens**[2,1], and **Zhen Xu**[1,2]

[1]Department of Biomedical Engineering, University of Michigan Ann Arbor

[2]Department of Pediatrics, Division of Pediatric Cardiology, University of Michigan, Ann Arbor, Michigan

Abstract

Histotripsy has shown promise in non-invasive cardiac therapy for neonatal and fetal applications. However for cardiac applications in general, and especially in the adult heart, cardiac and respiratory motion may affect the treatment accuracy and efficacy. This paper presents a histotripsy-mediated cardiac therapy system integrated with a fast motion-tracking algorithm and treatment monitoring using ultrasound imaging. Motion tracking is performed by diamond search block matching in real-time ultrasound images using a reference image of the moving target, refined by Kalman filtering. As proof of feasibility, this algorithm was configured to track 2D target motion and then electronically adjust the focus of a 1 MHz annular therapy array to correct for axial motion. This integrated motion tracking system is capable of sub-mm accuracy for displacements of 0–15 mm and velocities of 0–80 mm/s with a maximum error of less than 3 mm. Tissue phantom tests showed treatment efficiency and lesion size using motion tracking over displacements of 0–15 mm and velocities of 0–42 mm/s are comparable to those produced when treating stationary targets. *In vivo* validation was conducted in an open chest canine model, where the system provided 24 minutes of motion corrected histotripsy therapy in the live beating heart, generating a targeted lesion on the atrial septum. Based on this proof of feasibility and the natural extension of these techniques to three-dimensions, we anticipate a full motion correction system would be feasible and beneficial for non-invasive cardiac therapy.

Keywords

Histotripsy; Focused Ultrasound; Therapy; Motion Tracking

Introduction

Histotripsy produces fractionation of soft tissue based on precise control of cavitation (Xu et al. 2004; Parsons et al. 2006a; Roberts et al. 2006). Histotripsy has been successful in creating intra-cardiac communication in an open chest canine heart model (Xu et al. 2010), an intact neonatal porcine model (Owens et al. 2011, 2012), and an intact in utero fetal sheep model (Kim et al. 2011a). The perforations created in these studies generally have 1–4 mm

of hemorrhage surrounding the perforation. During these experiments, the heart motion perpendicular to the direction of ultrasound therapy propagation was small (< 2mm), while the heart motion along the direction of therapy propagation was sufficiently large (up to 17 mm) to move the septum out of the focal zone, resulting in reduced treatment efficiency and the potential for collateral damage. Furthermore, in cardiac applications involving adult hearts, such as atrial fibrillation, the cardiac motion will likely be significantly larger in both perpendicular and parallel directions to the ultrasound propagation. As such, the improved accuracy and efficiency motion correction provides will be increasingly necessary in order to reliably administer histotripsy therapy in these future applications.

Several target motion estimation and correction algorithms have been explored in conjunction with high intensity focused ultrasound (HIFU) therapy. Respiratory gating has been used to synchronize with HIFU applications to switch off therapy during breaths (Kubo and Hill 1996; Strickberger et al. 1999). More sophisticated approaches have also been developed to adjust the therapy focus to follow the target position in real-time. For example, ultrasound speckle tracking was employed to adjust the therapy focus to track the respiration motion using correlations of pulse-echo sequences from a subset of the transducers of the therapy phased array (Pernot et al. 2004; Marquet et al. 2011). Optical flow image processing techniques have also been utilized on real-time 2D ultrasound images for motion compensation in HIFU application (Auboiroux et al. 2012). Motion compensation was also investigated for magnetic resonance imaging (MRI) guided HIFU, such as the use of periodic respiratory motion and statistical models (Arnold et al. 2011; de Senneville et al. 2007; de Senneville et al. 2010; de Senneville et al. 2011) and tracking the target position in the image plane while compensating for the out-of-plane motion by dynamic slice tracking (Ries et al. 2010). These motion correction methods showed improvement in treatment efficiency and collateral damage reduction, but were mostly focused on treating slower moving abdominal organs.

The addition of fast cardiac motion on top of large respiratory motions significantly increases the complexity of tracking targets in the heart as opposed to tracking in other organs. Many algorithms have been developed for tracking cardiac motion in ultrasound imaging to evaluate heart function. These methods include myocardial border segmentation using deformable models (Jacob et al. 2002), myocardial motion and deformation estimation using phase shift estimation (D'hooge et al. 2002), spatio-temporal nonrigid registration with B-Spline interpolation (Ledesma-Carbayo et al. 2005), optical flow methods to compute local myocardial movements (Sühling et al. 2005), and block motion estimation and speckle tracking techniques (Kuo and von Ramm 2008). However, none have yet been combined to adjust the therapy focus in real-time for motion correction in an integrated ultrasound cardiac therapy system.

In this paper, we present a histotripsy-based cardiac therapy system integrated with real-time motion correction and treatment monitoring using ultrasound imaging. For this system, the motion correction must run at high frame rates due to the fast heart motion, and be robust against direct and indirect acoustic and electromagnetic interference from the high intensity histotripsy pulses. To address these challenges, we developed an ultrasound image-based motion tracking algorithm that utilizes a fast block matching technique, with real-time filtering for estimation error reduction. This algorithm was chosen due to its low computational requirements and ease of integration with the ultrasound image-guided histotripsy therapy system. In addition to the motion tracking capability, this integrated system has ultrasound imaging as real-time treatment monitoring that is free from interference of the therapy pulses. This integrated system was tested by performing two dimensional (2D) motion tracking based on ultrasound images and applying the motion feedback to correct for the one dimensional (1D) motion along the therapy axis by steering

the focus of the annular therapy array. In this initial study lateral motion correction was not performed based our previous experiments where communication through the atrial or ventricular septum (a membrane separating the two atria or ventricles) was generated for treatment of congenital heart diseases (Xu et al. 2010; Owens et al. 2011, 2012). In those studies, the axial motion (along the direction of ultrasound propagation) was observed to be the main motion of the atrial/ventricular septum, with only small motion in other directions. Due to the limitations of the hardware, 2D instead of three dimensional (3D) motion tracking was tested for this initial feasibility study. The integrated system developed here could potentially be upgraded to 3D by replacing the annular therapy array with a 2D phased array and replacing the 2D imaging probe with a 3D imaging probe.

In this paper, the performance of the current integrated system was evaluated in three steps *in vitro* followed by *in vivo* feasibility testing. First, to evaluate the tracking accuracy of the integrated system at different velocities, the actual movement path of the target was recorded by high speed optical images and compared with the estimated movement path from the algorithm. Second, to evaluate the treatment accuracy of the system, the size of the lesion created in moving tissue phantoms with the motion correction was compared to that produced without correction. Third, to investigate the efficiency of the system, the erosion rate produced with the motion correction in tissue phantoms and *ex vivo* porcine cardiac tissue was compared to that without correction. Finally, an *in vivo* feasibility experiment was conducted to determine the feasibility of integrating the algorithm into histotripsy therapy image guidance and targeting procedures.

Methods

Motion Tracking System Design

The motion tracking system we developed uses a custom algorithm to track a feature on ultrasound images using image processing techniques. This algorithm was integrated directly into the imaging sequence of an ultrasound imaging system. The imaging acquisition was synchronized with a 1 MHz histotripsy therapy array to minimize the interference of the therapy pulses on the ultrasound image. The imaging system's host computer processed the tracking algorithm and provided the results to the therapy array controller, updating the therapy focal position in real-time. Meanwhile, the treatment process was monitored through ultrasound imaging. The integrated system, consisting of the motion tracking algorithm, the ultrasound imaging system, and the histotripsy therapy system is described in detail below.

Ultrasound Imaging System—The ultrasound images were acquired by a Verasonics® Data Acquisition System (VDAS; Verasonics Inc., Redmond, WA, USA), interfaced with a Mac Pro desktop computer (Apple Inc., Cupertino, CA, USA), using an ATL HDI P7-4 (Philips, Andover, MA, USA), 5 MHz phased array imaging probe. This system was chosen for its high frame rate capabilities (by using a variable number of plane wave acquisitions) and flexible programmability allowing integration of processing algorithms within the imaging sequence.

To avoid interference from the histotripsy pulses, ultrasound image acquisitions were delayed 0.2 – 0.5 ms after the histotripsy pulses. Following this delay, image acquisition required 135 μs per steered plane wave acquisition (round-trip propagation time, which is dependent on the depth of the target). The number of plane wave acquisitions per image was chosen to balance sufficiently high image quality (spatial resolution) with a sufficiently high frame rate (temporal resolution). Though image quality could be improved by increasing the number of plane wave acquisitions per image, doing so reduced the overall frame rate. Therefore, while a single plane wave acquisition per image provided sufficient image quality

and a higher average frame rate (62 Hz) for motion tracking *in vitro*, 5 steered plane wave acquisitions were necessary for tracking in the *in vivo* experiment to achieve adequate imaging quality through the increased overlying tissue, reducing the average frame rate (31 Hz). Because of the low duty cycle (< 1%) used in histotripsy therapy pulses; the period between adjacent histotripsy pulses was sufficiently long to allow imaging acquisitions. Figure 1 shows a timing diagram example to illustrate the synchronization.

Motion Tracking Algorithm—Our real-time motion-tracking algorithm is based on tracking a distinguishable target feature on ultrasound images by comparison with a reference sub-image containing that target feature (reference block). First, the location of a moving target is identified in the current ultrasound image frame by finding the best match of the reference block in the current ultrasound frame using a block matching method. A reference image of the target is captured before therapy, which contains unique features or borders that can be distinguished from other structures in its vicinity. This reference block can be located within the therapy target region or nearby, provided the target region and reference feature move in unison, allowing the flexibility to track a prominent tissue feature but treat in another nearby location. The best matching block in the current frame in comparison to the reference block is identified by minimization of the sum of absolute difference (SAD) criterion. The error for a given location is found by subtracting the reference image from a block of the current frame centered at this potential new target location, and the absolute values of these pixel errors were summed to obtain the SAD (Equation 1).

$$SAD\left(i,j\right)=\sum_{x=1}^{N_x}\sum_{y=1}^{N_y}\left|ref\left(x,y\right)-image\left(i+x-\left[\frac{N_x}{2}\right],j+y-\left[\frac{N_y}{2}\right]\right)\right| \quad (1)$$

In this equation, the reference block "*ref*(·,·)" of size (N_x, N_y) is compared to the same-sized block surrounding the point (i,j) in the current image frame "*image*(·,·)".

To accelerate the computation, diamond search technique (Zhu and Ma 2000) was used to minimize search time in the current frame using knowledge of the target's position in the previous frame. First, to establish the initial position estimate on the first ultrasound frame, a single coarse search is performed over the entire frame. In subsequent frames, the diamond search procedure starts at the estimate from the previous frame, computing the SAD error for this location and those in a large diamond search pattern (LDSP) around it (Figure 2). Re-centering at the location among these with the lowest error, it computes the necessary additional SAD values to cover another LDSP around this point. This continues until the center point maintains the lowest SAD value, at which time a small diamond search pattern (SDSP) around that location produces the final estimate of the target position. This approach remains accurate so long as the overall frame rate is fast enough to keep the target's frame to frame motion small, thus ensuring the local minimum SAD corresponds to the target's new position.

The block matching estimate is filtered from frame to frame using a Kalman filter to reduce the interference of the noise on tracking. A need for filtering was based on early testing of the algorithm using ultrasound B-mode videos taken during *in vivo* experiments of two neonatal pigs and two fetal sheep. Without the Kalman filter, the estimated position within ultrasound videos was observed to jump around the actual position of the target rapidly. The addition of the Kalman filter removed this rapid fluctuation and improved tracking accuracy by an estimated 13%. Our implementation of the Kalman filter uses the horizontal and vertical positions ($h(n)$ and $v(n)$) and velocities ($h'(n)$ and $v'(n)$) as the current state, with the estimate of the current position equal to the previous position plus the previous velocity

times the time interval between frames (Δt). The system is assumed to be driven by changes in the velocity corresponding to samples of a zero-mean Gaussian random variable, $u(n)$ whose variances, ($\sigma_{u,h}$ and $\sigma_{u,v}$) must be estimated based on the expected target motion. The state equation for our Kalman filter is therefore:

$$\begin{bmatrix} h(n) \\ v(n) \\ h'(n) \\ v'(n) \end{bmatrix} = \begin{bmatrix} 1 & 0 & \Delta t & 0 \\ 0 & 1 & 0 & \Delta t \\ 0 & 0 & 1 & 0 \\ 0 & 0 & 0 & 1 \end{bmatrix} \cdot \begin{bmatrix} h(n-1) \\ v(n-1) \\ h'(n-1) \\ v'(n-1) \end{bmatrix} + \begin{bmatrix} 0 & 0 \\ 0 & 0 \\ 1 & 0 \\ 0 & 1 \end{bmatrix} \cdot u(n) ; u(n) \tilde{\ } N \left(\begin{bmatrix} 0 \\ 0 \end{bmatrix}, \begin{bmatrix} \sigma_{u,h} & 0 \\ 0 & \sigma_{u,v} \end{bmatrix} \right) \quad (2)$$

Observation of the system is through estimates of the horizontal and vertical positions from our block matching algorithm ($\bar{h}(n)$ and $\bar{v}(n)$). These estimates are assumed to be accurate, but corrupted by zero-mean Gaussian noise, $w(n)$ whose variances, ($\sigma_{w,h}$ and $\sigma_{w,v}$) must be determined based on the current imaging quality. The observation equation for our Kalman filter is therefore:

$$\begin{bmatrix} \bar{h}(n) \\ \bar{v}(n) \end{bmatrix} = \begin{bmatrix} 1 & 0 & 0 & 0 \\ 0 & 1 & 0 & 0 \end{bmatrix} \cdot \begin{bmatrix} h(n) \\ v(n) \\ h'(n) \\ v'(n) \end{bmatrix} + w(n) ; w(n) \tilde{\ } N \left(\begin{bmatrix} 0 \\ 0 \end{bmatrix}, \begin{bmatrix} \sigma_{w,h} & 0 \\ 0 & \sigma_{w,v} \end{bmatrix} \right) \quad (3)$$

For a given scenario, the variances of the driving force and observation noise are the only independent variables and must be tuned by analyzing video and tracking performance of the system in each individual treatment, before delivering histotripsy therapy. The Kalman filter recursion then produces the final estimate of the new target position based on a weighted average of the result of the search algorithm with an estimate of where the target should be based on its previous position and velocity. This final position estimate is then passed through a custom 1 MB/sec universal serial bus (USB) communication link (FT245BL, Future Technology Devices International Ltd., Glasgow, UK) to the histotripsy therapy array controller to adjust the therapy focus to the target's new estimated position in less than 1 ms.

Histotripsy Therapy System—Histotripsy therapy was delivered by a 1 MHz high power ultrasound annular array transducer (Imasonic, SA, Besançon, France). This transducer is composed of 16 equal-area ring elements aligned confocally on a spherical segment, allowing axial focal steering. The transducer had a 100mm aperture and was geometrically focused at 90mm (f# = 0.9), with a 40mm central hole to accommodate an imaging probe. The annular array was driven by custom hardware, implemented on a field programmable gate array (FPGA, Cyclone II, Altera Corp., San Jose, CA, USA) with USB connectivity to control the ultrasound therapy output parameters in real-time. Focal patterns for axial foci between 80 and 100 mm with 0.5 mm spacing between adjacent foci were programmed and stored in the FPGA. During therapy, the therapy controller can then change the transducer focus position to any position within these pre-programmed locations in less than 1 ms. This driver output was then routed to custom high-power amplifiers built in-house and electronically matched to the load transducer.

In all *in vitro* experiments, the transducer was driven at the same input voltage level, corresponding to peak negative/positive pressures of −21.2/88.5 MPa in free field at the geometric focus. This was measured with a fiber optic probe hydrophone (Parsons et al. 2006b). A pulse duration of 3 cycles was used for calibration to prevent cavitation at the fiber tip, while still achieving the same peak pressures as longer pulses since the transducer

ring up period comprises 3 cycles. An example of measured pressure waveform is shown in Figure 3a. The effect of axial focus steering on the pressure is illustrated in Figure 3b, where the ratio of the peak negative pressure level relative to that at the geometric focus (90mm) ranges from about 1.06 at 80 mm to 0.88 at 100 mm.

In Vitro Tissue Phantom Validation

This integrated histotripsy therapy system was then tested in three *in vitro* scenarios using tissue mimicking gel phantoms to measure the impact of the motion tracking algorithm on the accuracy and efficiency of histotripsy therapy. First, to evaluate the accuracy at different tracking velocities, the target position estimates from the algorithm were compared to the position of the target measured from optical images of the moving target during therapy. The optical images were taken at high resolution (30μm pixel size) with a short exposure (2 μs) to provide an accurate measurement of the target movement. Second, to evaluate the treatment accuracy and collateral damage reduction, the lesion dimensions created in moving phantoms with the tracking algorithm were compared to those produced without tracking. Third, to investigate the efficiency of the system, the erosion rate (defined as the thickness of the phantom divided by the time required to perforate it) in tissue phantoms treated with the tracking algorithm enabled were compared to those treated without tracking enabled.

System Tracking Accuracy at Different Velocities—To quantify the motion tracking system accuracy, the path of the target was measured by imaging the target phantom location using a high speed camera (Phantom V210, Vision Research Inc., Wayne, NJ, USA). High resolution images of the target phantom's range of motion were captured through a telephoto lens assembly, resulting in a resolution of ~30 microns per pixel. These synchronized images were acquired 60 μsec after the therapy pulse firing to account for the acoustic propagation time. The images were then post-processed to produce the reference target path for error quantification by comparison with the estimated path stored in the therapy controller.

The target was a 0.18 mm diameter nylon line target embedded in a 1% agarose hydrogel inside an acetal housing. This phantom was moved using a Parker XRS positioning system (Parker Hannifin Corp., Mayfield Heights, Ohio, USA) over a 15 mm linear path along the therapy axis with constant acceleration magnitude of 400 mm/s^2 and maximum velocities between 10 and 80 mm/s to test the upper limits of the tracking capabilities of the algorithm. Varying the pulse duration and pulse repetition frequency (PRF) over the typical histotripsy therapy ranges had no effect on the motion tracking frame rate, and therefore accuracy was tested only for a single pulse duration and PRF in this study. Histotripsy was delivered using 5 cycle pulse duration and 500 Hz PRF for 10 seconds at each of the tested velocities. The estimated path was downloaded after each experiment from the FPGA board. The difference between the estimated path and path recorded from the high speed images was computed as the tracking error.

System Treatment Accuracy – Lesion Size—To quantify the treatment accuracy of the system, the sizes of lesions generated in a moving tissue phantom with and without the motion tracking system as well as a stationary control phantom were measured and compared. The phantom was moved along the therapy axis, and histotripsy therapy was applied to the phantom both with and without motion correction. The initial resting position of the line target was aligned with the geometric focus of the therapy transducer. Motion was programmed using the Parker XRS positioning system, with constant acceleration of 60 mm/s^2 over displacements of 5, 10, and 15 mm centered at the geometric focus of the therapy transducer. These corresponded to maximum velocities of approximately 24, 34, and

42 mm/s respectively. We could not reliably secure the gel phantom at higher accelerations and velocities because the phantom would slide out of its housing at higher velocities. The velocities tested here are sufficient to represent the majority of physiological organ motion ranges, and provide complementary data to the raw accuracy assessment described previously. Control experiments were conducted with no phantom motion and the target line placed at the geometric focus.

A tissue-mimicking agarose gel phantom with an embedded red blood cell (RBC) layer was used here to identify the lesion size, because it was shown to produce reliable estimates of the cavitation-induced damage zone. In this phantom, The RBC area lysed by histotripsy changed from opaque red to translucent pink (Maxwell et al. 2010), allowing direct visualization and evaluation of the lesion size. In this experiment, a 5% RBC layer in a 1% agarose gel phantom was made using the methods described in the paper by Maxwell et al. (2010). The lesions in the treated phantoms were photographed and post-processed to quantify the length and area of the lesion. The images were segmented using a local intensity threshold to distinguish the lighter treated lesion areas from the darker, intact red blood cells surrounding the lesions. The length and area of the lesions generated with and without motion tracking were computed and normalized by the length and area of the corresponding control lesion to allow fair comparison between samples. The methods to segment the lesion and calculate the length and area of the lesion are detailed in Maxwell et al. (2010).

In this experiment series, a line target was embedded perpendicular to the RBC layer to provide a distinguishable target in the otherwise acoustically uniform gel phantom. Histotripsy pulses at 10 cycle duration and 50 Hz PRF were applied for 2 minutes. This parameter combination was used because it has achieved effective fractionation in RBC phantoms in previous experiments (Maxwell et al. 2010).

System Treatment Efficiency – Erosion Rate—To evaluate the efficiency of the integrated system, the rate at which a moving gel phantom layer was perforated (erosion rate) using histotripsy with and without tracking was measured and compared (sample size = 3). To mimic an *in vivo* scenario where the perforation in the atrial or ventricular septum in the heart was generated using histotripsy a mobile tissue membrane phantom between two fluid chambers was developed. Agarose gel at 2.5% concentration by weight was formed into discs roughly 3–4 mm thick and 30 mm in diameter, with graphite embedded in the gel at 2% concentration to provide both ultrasound speckle and visualization of lesion generation. The gel disc was adhered over the center hole of a latex membrane sealing the top of a hollow cylindrical chamber (Figure 4), allowing direct fluid access on both sides of the gel disc. A pulsatile pump (Model 1423, Harvard Apparatus, Holliston, MA) was linked to the chamber to pump water into and out of the sealed cylinder, displacing the gel phantom, mimicking the *in vivo* cardiac tissue motion. The displacement and velocity could be tuned by adjusting the stroke volume and stroke rate of the pump, resulting in movement strictly along the therapy axis between 3 and 12.5 mm at speeds up to 60 mm/s. Movements of 3, 5, 7, 10 and 12.5 mm at a maximum velocity of 40 mm/s were used.

To quantify erosion rate, the phantoms were treated with 5 cycle histotripsy pulses at 1 kHz PRF to mechanically erode the proximal surface of the gel phantom, expelling the fractionated gel and graphite fragments into the surrounding liquid, eroding a visible flow channel through the phantom. These parameters were chosen as they have been used to successfully generate perforation in the atrial or ventricular septum in the heart in our previous *in vivo* studies (Owens et al. 2011, 2012). The erosion rate was computed as the thickness of the gel membrane phantom divided by treatment time required to create a visible channel through the opaque gel phantom. Control experiments were performed with

the same setup with no phantom motion. The erosion rates produced with and without motion correction were compared at identical displacements.

Ex Vivo Tissue Validation

To validate the *in vitro* erosion rate results, a proof of concept experiment was conducted with excised porcine atrial wall tissue. The tissue was harvested from fresh porcine hearts obtained from a local supplier on the day of the experiment. Four samples of approximately 10 by 20 mm were mounted to the same apparatus as the *in vitro* erosion rate experiment (Figure 4), with the pump stroke volume set to achieve a maximum motion displacement of 10 mm. Three locations (separated by 8 mm laterally) on each tissue sample were exposed to 5 cycle histotripsy pulses at 1 kHz PRF. Three scenarios were tested: control with no motion, motion without tracking, and motion with tracking. Histotripsy therapy was applied until perforation was achieved, with the treatment time and resulting erosion rate recorded.

In Vivo Feasibility

The procedures described here were reviewed and approved by the University Committee on Use and Care of Animals at the University of Michigan (UCUCA). For *in vivo* proof of feasibility, the system was tested on tracking and treating the atrial septum in a single animal open-chest canine heart model. Although the ultimate clinical application would be non-invasive (either transcostal or subcostal acoustic windows) and not require surgery, this animal model and setup were used previously (Xu et al. 2010) for atrial septal defect (ASD) creation (perforation through the atrial septum) using histotripsy and was suitable to test the motion tracking system. A motion range (5.2 to 17.1 mm axial displacement) was observed previously for the atrial septum. Therapy access to the heart was achieved through a midline sternotomy with retraction of the ribcage. The lungs were retracted laterally to prevent interference with ultrasound propagation and the pericardium was left intact. A temperature-controlled, degassed water bath enclosed in a thin plastic bag was coupled to the pericardium with ultrasound gel. The coaxially mounted imaging and therapy transducers were submerged in the water bath outside the heart, and positioned under ultrasound guidance to center the geometric focus of the transducer over the approximate center of the atrial septum's motion path. A reference image of the atrial septum was acquired prior to the histotripsy therapy and used to set up initial motion tracking parameters. After the motion tracking algorithm and parameters were tuned, histotripsy pulses of 5 cycles at 1 kHz PRF were applied for 10 exposures at 3 different locations on the front, middle and back of the atrial septum, totaling 24 minutes of therapy.

Results

Motion Tracking System Performance

The integrated motion correcting histotripsy therapy system achieved a maximum frame rate of 62 Hz. The system is capable of tracking targets up to the highest velocity (80 mm/s) and highest acceleration (400 mm/s^2) tested. The status of the motion tracking was monitored by the operator in real-time through an overlay of the estimated target position on the ultrasound image. In two cases of the 15 erosion rate trials, and in three of 10 individual treatments in the *in vivo* study, the system encountered significant out-of-plane motion, imaging artifacts or other anomalies resulting in a loss of target tracking, in which cases the operator immediately halted therapy and reset the tracking to the intended target.

In Vitro Tissue Phantom Validation

System Accuracy vs. Tracking Velocity—Estimated paths from the motion tracking system and the measured paths taken from the high speed camera were collected at 500 Hz

PRF therapy at a fixed acceleration magnitude of 400 mm/s^2 and velocities between 10 and 80 mm/s. The root mean squared (RMS) and maximum error between the two paths over 10 second captures for each scenario is presented in Table 1. The RMS accuracy for the motion tracking system over the tested velocity range was 0.52 mm, which is very close to the 0.5 mm step size of the therapy focus steering.

An example plot of the estimated path versus the measured path is shown in Figure 5 for two velocity scenarios. At lower velocities error is dominated by the steering step size, as the transducer was only programed with foci at 0.5 mm separations, producing an RMS error less than 0.51 mm. This focal step size could be arbitrarily decreased to reduce this source of error, however this was not practically necessary since 0.5 mm is already small compared to the bubble cloud's axial extent (25 mm). At higher velocities, the error is above the 0.5 mm step size with RMS error up to 0.66 mm at 80 mm/s velocity, with the estimated position trailing the actual path in time. At these high velocities, the motion during the algorithm processing time latency (averaging 16 ms) between image acquisition and the resulting focal update becomes substantial, increasing tracking error.

System Accuracy - Lesion Size—The area and length of the lesions created by the histotripsy system in a moving gel phantom with and without using motion correction were measured. Lesion area and length data were collected for 3 samples at each of the displacements 5, 10, and 15 mm. The lesion images were segmented using local pixel intensity thresholds; an example image before and after segmentation is shown in Figure 6.

From these segmented images, the area and length of motion tracking and no tracking lesions were computed as percentages of the dimensions relative to their corresponding control lesion (Figure 7). The area and length of the lesions generated in the moving targets using motion tracking were comparable to those generated with stationary targets. The mean percentages of the lesion areas with respect to the control lesion were 93.0%, 100.0%, and 92.0% using motion tracking at displacements of 5, 10, and 15 mm, respectively. Similarly, the mean percentages of the lesion lengths with respect to the control lesion were 99.2%, 100.0%, and 88.8% using motion tracking at displacements of 5, 10, and 15 mm, respectively. In comparison, the lesions generated without motion tracking were significantly larger, and the total lesion area and length increased with increasing displacement. The mean percentages of the lesion areas with respect to the control lesion were 128.5%, 166.5% and 194.1% without motion tracking at displacements of 5, 10, and 15 mm, respectively. The mean percentages of the lesion lengths with respect to the control lesion were 137.9%, 166.7% and 197.6% without motion tracking at displacements of 5, 10, and 15 mm, respectively. T-tests show that both the lesion area and length without motion tracking are significantly larger than their corresponding control lesion ($p < 0.05$), while lesion area and length with motion tracking are not significantly larger than their corresponding control lesion ($p > 0.3$).

System efficiency - Erosion Rate—The erosion rate of a 2.5% agarose hydrogel membrane phantom was computed for each of the motion displacements 3, 5, 7.5, 10, and 12.5 mm with and without motion tracking (N = 3). Control experiments were conducted without motion (N = 3) resulting in an erosion rate of 3.03±0.14 mm/min, representing the maximum erosion rate for this scenario. A plot of erosion rate versus motion range is presented in Figure 8. A two-sample t-test shows that the erosion rate with motion tracking was significantly higher than the erosion rate without motion tracking ($p < 0.05$) for all displacements. Erosion rate with tracking for all displacements averaged 2.7±0.29 mm/min, or approximately 89.0% of the control rate ($p < 0.05$). Without tracking, erosion rate was substantially reduced to between 1.8±0.07 mm/min for the 3 mm displacement (61.6% of the control rate) and 0.91±0.14 mm/min for the 12.5 mm displacement (30.0% of the control

rate) ($p < 0.05$). Differences in erosion rate among the individual displacements for the motion tracking case were not significant ($p > 0.05$), except between the 3 mm and 7.5 mm displacements ($p = 0.03$) due to a low observed variance in those specific samples.

Ex Vivo Tissue Validation Results

Erosion rate in *ex vivo* atrial wall tissue was measured for a 10 mm motion range (N = 4). An erosion rate of 4.51±0.89 mm/min was achieved for the control case (stationary target). Erosion rate with motion tracking was measured at 4.40±0.82 mm/min which was comparable to the control rate, ($p = 0.86$; t-test; 97% of control rate). Erosion rate without motion tracking was measured at 1.90±0.39 mm/min or 42% of the control rate, which was significantly lower than both the control and motion tracking rates ($p < 0.01$; t-test).

In Vivo Feasibility Results

In the *in vivo* experiment, the motion tracking system successfully tracked the motion of the atrial septum in the live beating canine heart at 3 separate locations. The atrial septum was observed to move over a maximum displacement of 8 mm due to the 14.1±2.1 breaths per minute respiration and 116.6±11.0 beats per minute heart rate. A frame rate of 32.6±5.6 Hz was achieved for accurate motion tracking, which was lower than that in the *in vitro* case due to the increased imaging time required for the 5 steered plane wave acquisitions needed to improve imaging quality. An excerpt of the estimated target path recorded during treatment is plotted in Figure 9. The path shows the expected short, quick movements of the septum from cardiac motion added with the larger, slower movements from respiration. 10 treatments totaling 24 minutes of therapy were applied to the septum, generating a targeted lesion on the atrial septum as shown by ultrasound in Figure 10. Since this was a procedural feasibility study, the animal was euthanized immediately following therapy. Histological confirmation of a lesion created by histotripsy is shown in the Hematoxylin and Eosin (H&E) stained slide of the treated atrial septum (Figure 11). Distinctive borders of injury and slight areas of flanking hemorrhage at the boundary were observed. Wound healing and long-term effects of therapy could not be evaluated with this study.

Discussion and Conclusion

This study has been our first attempt to integrate a motion correction scheme into a histotripsy system to track the motion of a cardiac target during histotripsy therapy. Our results indicate that the block matching method using diamond search algorithm and Kalman filtering is capable of tracking fast motion with high accuracy. When treating a moving target *in vitro*, significant improvement in therapy accuracy and efficiency was achieved compared to therapy without using the algorithm. Though *in vitro* testing phantoms could not produce the non-rigid motion present in the heart, feasibility was evaluated in a live beating heart *in vivo* with further work necessary to quantitatively evaluate the system performance in this setting and adapt the system for non-invasive therapy.

The main advantage of the system developed here over previously developed ultrasound therapy system with motion correction is that it requires no specialized hardware for implementation. To implement a system similar to the successful motion correcting ultrasound therapy systems demonstrated previously by Pernot et al. (2004) and Marquet et al. (2011), a 2D phased array therapy system with both transmit and receive capabilities would have to be developed along with corresponding multi-channel data-acquisition hardware. Similar to another recently developed motion correction system (Auboiroux et al. 2012) our integrated therapy motion correction utilized ultrasound images directly for target motion tracking. The optical flow techniques from that work are aimed at slower moving abdominal organs, and the resulting lower frame rates (8 Hz) are likely not sufficient for

high speed cardiac motion. Another advantage of reference image or landmark based tracking methods like these is that they allow the flexibility to utilize image features that are arbitrarily shaped and positioned, and avoids the risk of error compounding over time inherent in relative motion tracking methods. For example, frame to frame speckle tracking methods can allow small estimation errors from each frame to compound over time, potentially degrading accuracy over time as the tracked location "drifts". Our method uses a single reference image for all motion estimates, where the reference feature is either found and the system remains accurate, or an easy to identify tracking error occurs, and therapy can be halted. If the tracked feature is within the treated volume, however, the reference image will need to be recaptured as the treatment progresses, as the appearance of the reference will change when that volume is fractionation by histotripsy.

The current system is not without limitations. In this study, the algorithm tracks the motion in 2D based on ultrasound images, while therapy focus steering is only performed in the axial dimension. This limited dimensionality is useful for correcting the motion encountered in the neonatal and fetal cardiac applications that we are currently investigating, where the only significant motion is along the therapy axis. However, future applications in the adult heart will likely require 3D motion correction. Extensions of the key components of our system (diamond search, SAD criterion, and Kalman filtering) to a 3D motion correction system are straightforward with the use of 3D ultrasound data or two orthogonal 2D image planes. Though computational complexity is the major concern for the extension of the block matching method, it potentially can be mitigated with appropriate choices of imaging field of view, reference block size, and search procedure. For example, a potential 3D Diamond Search pattern would only require 19/6 test points in LDSP/SDSP versus the current 9/4 in 2D. Furthermore, processing hardware upgrades and computation parallelization may potentially offset these additional requirements, and we anticipate sufficiently high maximal tracking velocity can be achieved for cardiac therapy. Other 3D ultrasound motion tracking methods have been demonstrated (Harris et al. 2007; Bell et al. 2012), and will be evaluated as potential alternatives to the proposed block matching estimation for improved tracking of the non-rigid motion of heart structures. With these improvements, the system's performance could be more directly compared with previous work on 3D motion correction for ultrasound therapy and evaluated for its utility in high speed targets for cardiac therapy.

Other improvements, intended to enhance clinical applicability and ease of use, include automatically halting therapy when tracking is lost, as detected by the SAD metric dropping below a threshold value. Also, as the cavitation bubble cloud is the effective "scalpel" in histotripsy treatment, an algorithm incorporating simultaneous bubble cloud tracking will help evaluate the effectiveness and accuracy of the motion tracking during histotripsy therapy. More precise adjustments could then be made based on this feedback to further improve the therapy efficiency and accuracy if necessary.

The *in vivo* experiment used an open-chest adult canine model, which provided cardiac motion for our feasibility study. Our current goal is to implement the motion tracking method for pediatric cardiac applications, including perforation of the atrial septum in the neonatal patients with hypoplastic left heart syndrome (HLHS). In these pediatric patients, a subcostal acoustic window exists to access the atrial setup without lung or rib obstruction. Unfortunately this acoustic window does not exist in non-primate animals, as their heart orientation is different from humans. We have utilized transthoracic histotripsy to create cardiac lesions in neonatal animal models, but partial lung and rib obstruction was encountered (Owens et al. 2011, 2012). Even though histotripsy has been shown to be able to generate precise lesions through ribs without aberration correction (Kim et al. 2011b), the lungs full of air in the ultrasound pathway still pose a serious problem. Therefore, to access

the atrial septum, an open-chest surgery was performed in this initial feasibility study. In the future, we plan to augment the animal model to create access to the atrial septum through an intact chest (e.g., by filling the lung with fluid), which will allow us to test non-invasive histotripsy cardiac therapy integrated with motion tracking without the need to perform open-chest surgery. In addition, to further improve the imaging quality, we also plan to redesign our therapy transducer to allow the imager to be directly placed on to the patient's skin to avoid imaging quality degradation caused by stand-off distance between the imager and the skin. With all these improvements, this motion tracking system can be a valuable tool for histotripsy therapy on moving targets, such as cardiac applications to create intra-cardiac communications in infants with congenital heart disease or the removal of excess myocardial tissue such as that found in adult patients with hypertrophic cardiomyopathy.

Acknowledgments

References

Arnold P, Preiswerk F, Fasel B, Salomir R, Scheffler K, Cattin P. 3D Organ Motion Prediction for MR-guided High Intensity Focused Ultrasound. Med Image Comput Comput Assist Interv. 2011; 14(Pt 2):623–630. [PubMed: 21995081]

Auboiroux V, Petrusca L, Viallon M, Goget T, Becker CD, Salomir R. Ultrasonography-based 2D motion-compensated HIFU sonication integrated with reference-free MR temperature monitoring: a feasibility study ex vivo. Phys Med Biol. 2012; 57(10):N159–N171. [PubMed: 22517112]

Bell MA, Byram BC, Harris EJ, Evans PM, Bamber JC. In Vivo Liver Tracking with a High Volume Rate 4D Ultrasound Scanner and a 2D Matrix Array Probe. Phys Med Biol. 2012; 57(5):1359–1374. [PubMed: 22349408]

de Senneville BD, Mougenot C, Moonen CT. Real-Time Adaptive Methods for Treatment of Mobile Organs by MRI-Controlled High-Intensity Focused Ultrasound. Magn Reson Med. 2007; 57(2):319–330. [PubMed: 17260361]

de Senneville BD, Ries M, Maclair G, Moonen C. MR-Guided Thermotherapy of Abdominal Organ Using a Robust PCA-Based Motion Descriptor. IEEE Trans Med Imaging. 2011; 30(11):1987–1995. [PubMed: 21724501]

de Senneville BD, Roujol S, Moonen C, Ries M. Motion Correction in MR Thermometry of Abdominal Organs: a Comparison of the Referenceless vs. the Multibaseline Approach. Magn Reson Med. 2010; 64(5):1373–1381. [PubMed: 20677237]

D'hooge J, Konofagou E, Jamal F, Heimdal A, Barrios L, Bijnens B, Thoen J, Van de Werf F, Sutherland G, Suetens P. Two dimensional ultrasonic strain rate measurement of the human heart in vivo. IEEE Trans Ultrason Ferroelectr Freq Control. 2002; 49(2):281–286. [PubMed: 11885685]

Harris EJ, Miller NR, Bamber JC, Evans PM, Symonds-Tayler JR. Performance of Ultrasound Based Measurement of 3D Displacement Using a Curvilinear Probe for Organ Motion Tracking. Phys Med Biol. 2007; 52(18):5683–5703. [PubMed: 17804889]

Jacob G, Noble AJ, Behrenbruch C, Kelion AD, Banning AP. A shape-space-based approach to tracking myocardial borders and quantifying regional left-ventricular function applied in echocardiography. IEEE Trans Med Imaging. 2002; 21(3):226–238. [PubMed: 11989847]

Kim Y, Gelehrter SK, Fifer CG, Lu JC, Owens GE, Berman DR, Williams J, Wilkinson JE, Ives KA, Xu Z. Non-invasive pulsed cavitational ultrasound for fetal tissue ablation: feasibility study in a fetal sheep model. Ultrasound Obstet Gynecol. 2011; 37(4):450–457. [PubMed: 21433165]

Kim Y, Wang TY, Xu Z, Cain CA. Lesion generation through ribs using histotripsy therapy without aberration correction. IEEE Trans Ultrason Ferroelectr Freq Control. 2011; 58(11):2334–2343. [PubMed: 22083767]

Kubo HD, Hill BC. Respiration gated radiotherapy treatment: a technical study. Phys Med Biol. 1996; 41(1):83–91. [PubMed: 8685260]

Kuo J, von Ramm OT. Three-dimensional Motion Measurements Using Feature Tracking. IEEE Trans Ultrason Ferroelectr Freq Control. 2008; 55(4):800–810. [PubMed: 18467224]

Ledesma-Carbayo MJ, Kybic J, Desco M, Santos A, Sühling M, Hunziker P, Unser M. Spatio-Temporal Nonrigid Registration for Ultrasound Cardiac Motion Estimation. IEEE Trans Med Imaging. 2005; 24(9):1113–1126. [PubMed: 16156350]

Marquet F, Aubry JF, Pernot M, Fink M, Tanter M. Optimal transcostal high-intensity focused ultrasound with combined real-time 3D movement tracking and correction. Phys Med Biol. 2011; 56(22):7061–7080. [PubMed: 22016152]

Maxwell AD, Wang TY, Yuan L, Duryea AP, Xu Z, Cain CA. A Tissue Phantom For Visualization and Measurement of Ultrasound-Induced Cavitation Damage. Ultrasound Med Biol. 2010; 36(12): 2132–2143. [PubMed: 21030142]

Owens GE, Miller RM, Ensing G, Ives K, Gordon D, Ludomirsky A, Xu Z. Therapeutic Ultrasound to Noninvasively Create Intracardiac Communications in an Intact Animal Model. Catheter Cardiovasc Interv. 2011; 77(4):580–588. [PubMed: 20853366]

Owens GE, Miller RM, Owens ST, Swanson SD, Ives K, Ensing G, Gordon D, Xu Z. Intermediate-Term Effects of Intracardiac Communications Created Noninvasively by Therapeutic Ultrasound (Histotripsy) in a Porcine Model. Pediatr Cardiol. 2012; 33(1):83–89. [PubMed: 21910018]

Parsons JE, Cain CA, Abrams GD, Fowlkes JB. Pulsed Cavitational Ultrasound Therapy for Controlled Tissue Homogenization. Ultrasound Med Biol. 2006; 32(1):115–129. [PubMed: 16364803]

Parsons JE, Cain CA, Fowlkes JB. Cost-effective Assembly of a Basic Fiber-optic Hydrophone for measurement of High-Amplitude Therapeutic Ultrasound Fields. J Acoust Soc Am. 2006; 119(3): 1432–1440. [PubMed: 16583887]

Pernot M, Tanter M, Fink M. 3-D Real-Time Motion Correction in High-Intensity Focused Ultrasound Therapy. Ultrasound Med Biol. 2004; 30(9):1239–1249. [PubMed: 15550328]

Ries M, de Senneville BD, Roujol S, Berber Y, Quesson B, Moonen C. Real-Time 3D Target Tracking in MRI Guided Focused Ultrasound Ablations in Moving Tissues. Magn Reson Med. 2010; 64(6): 1704–1712. [PubMed: 20878763]

Roberts WW, Hall TL, Ives K, Wolf JS, Fowlkes JB, Cain CA. Pulsed Cavitational Ultrasound: A Noninvasive Technology for Controlled Tissue Ablation (Histotripsy) in the Rabbit Kidney. J Urol. 2006; 175(2):734–738. [PubMed: 16407041]

Strickberger SA, Tokano T, Kluiwstra JU, Morady F, Cain CA. Extracardiac Ablation of the Canine Atrioventricular Junction by Use of High-Intensity Focused Ultrasound. Circulation. 1999; 100(2): 203–208. [PubMed: 10402451]

Sühling M, Arigovindan M, Jansen C, Hunziker P, Unser M. Myocardial Motion Analysis From B-Mode Echocardiograms. IEEE Trans Image Process. 2005; 14(4):525–536. [PubMed: 15825486]

Xu Z, Ludomirsky A, Eun LY, Hall TL, Tran BC, Fowlkes JB, Cain CA. Controlled Ultrasound Tissue Erosion. IEEE Trans Ultrason Ferroelectr Freq Control. 2004; 51(6):726–736. [PubMed: 15244286]

Xu Z, Owens G, Gordon D, Cain C, Ludomirsky A. Noninvasive Creation of an Atrial Septal Defect by Histotripsy in a Canine Model. Circulation. 2010; 121(6):742–749. [PubMed: 20124126]

Zhu S, Ma KK. A New Diamond Search Algorithm for Fast Block-Matching Motion Estimation. IEEE Trans Image Process. 2000; 9(2):287–290. [PubMed: 18255398]
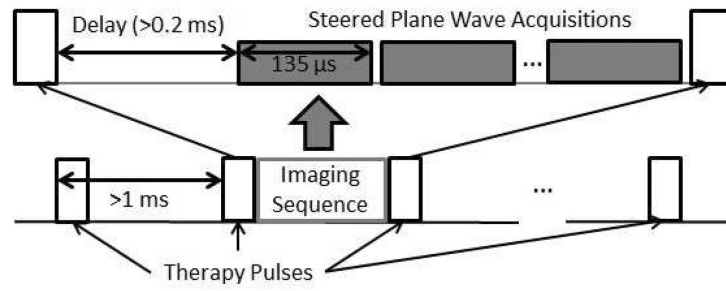
Figure 1.
Timing diagram illustrating the synchronization and integration of the imaging sequence between therapy pulses with typical parameters.
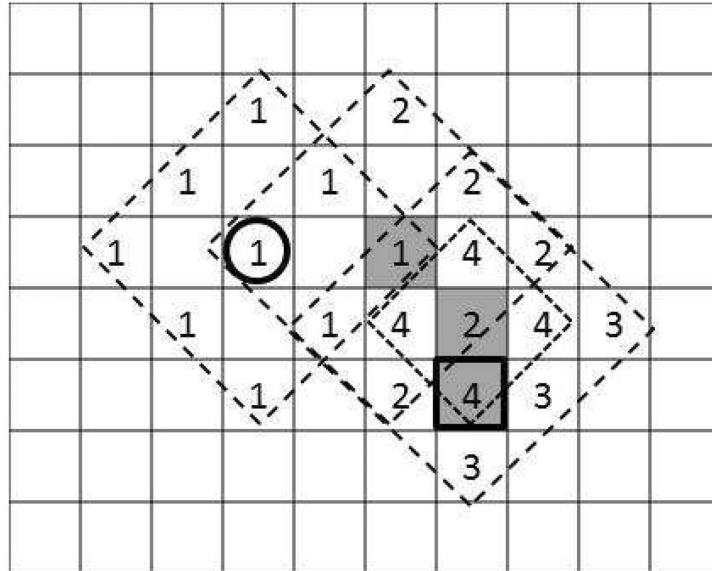
Figure 2.
Illustration of the diamond search procedure: starting from the previous target position (bold circle), successive LDSP iterations (1–3) are computed with the best match of each shaded gray. Once the center location remains the best match (shaded "2" remained best match on iteration 3), the SDSP locations (4) are tested and the best match is the new estimate of the target's position (bold square).
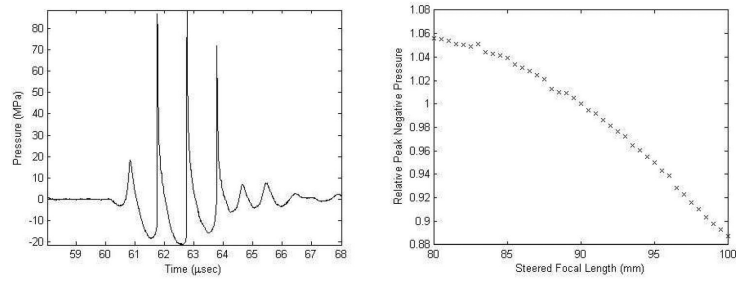
Figure 3.
Pressure calibration plots for the therapy transducer. a) Pressure waveform for a 3-cycle pulse at the output pressure level used *in vitro* and measured at the geometric focus (90 mm). b) Peak negative pressure over the axial steering range relative to that at the geometric focus.
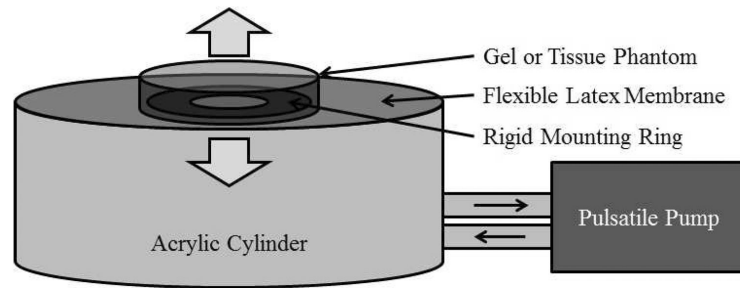
Figure 4.
Diagram of the phantom apparatus used to evaluate erosion rates. Water was pumped into and out of an acrylic cylinder, flexing the latex membrane top, creating motion along the axis of the cylinder. A gel or tissue sample was adhered over the center hole of a rigid mounting ring in the center of the latex top.
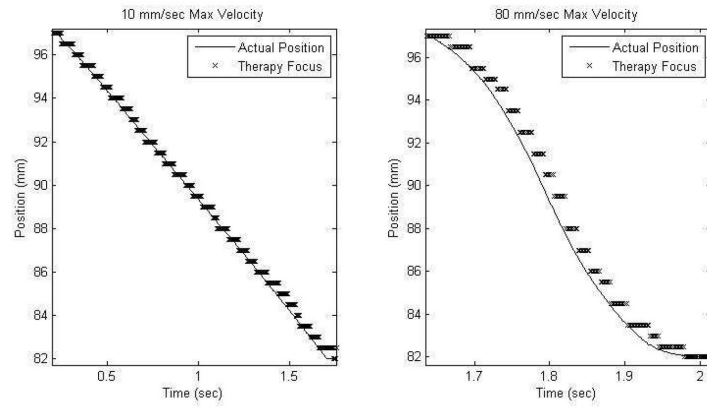
Figure 5.
Plots of the estimated and actual motion paths for 10 and 80 mm/s velocities
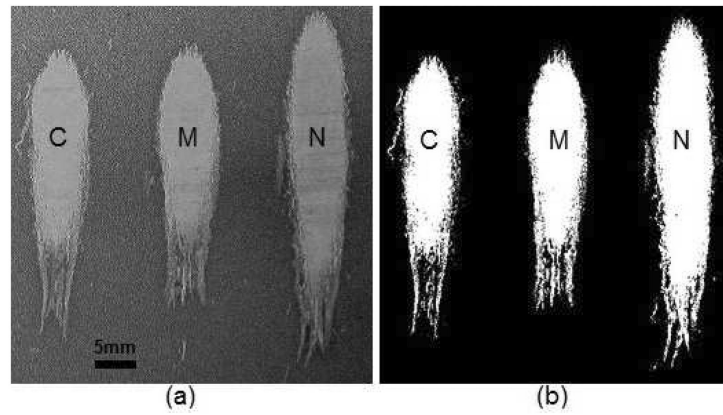
Figure 6.
Lesion image before (panel a) and after (panel b) threshold image segmentation showing, from left to right: control (C), motion tracking (M), and no tracking (N) lesions for a displacement of 5 mm.
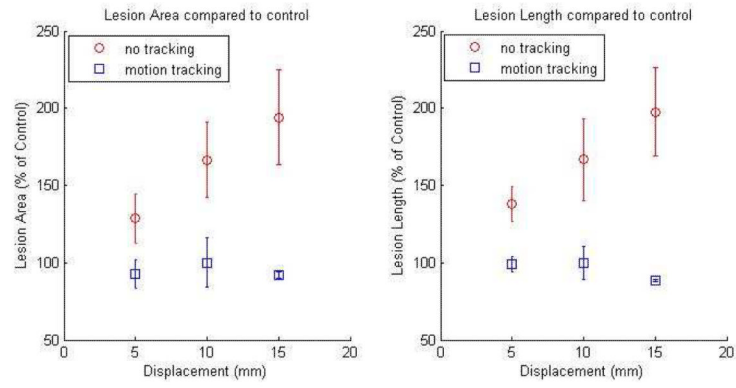
Figure 7.
Lesion area and length compared to control (% of the control) versus target displacement for lesions generated with motion tracking (square) and without motion tracking (diamond).
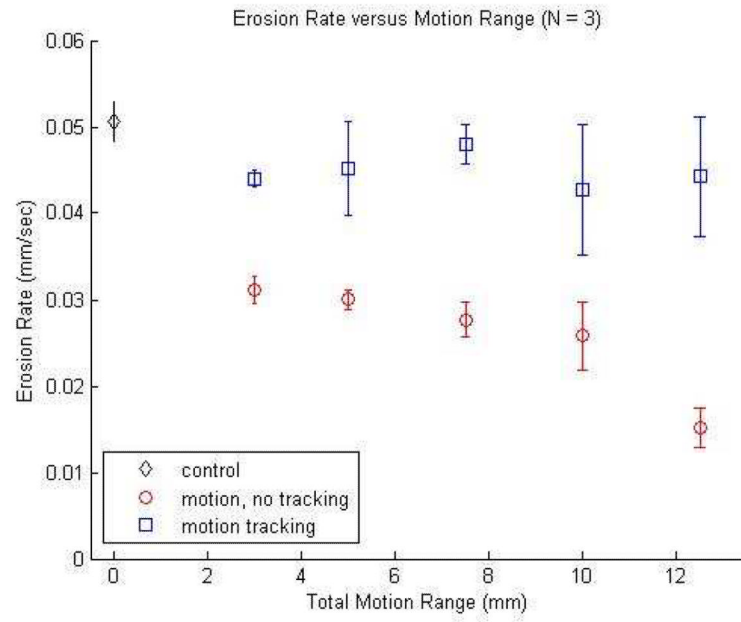
Figure 8.
Erosion rate versus target phantom displacement for control without motion (diamond),
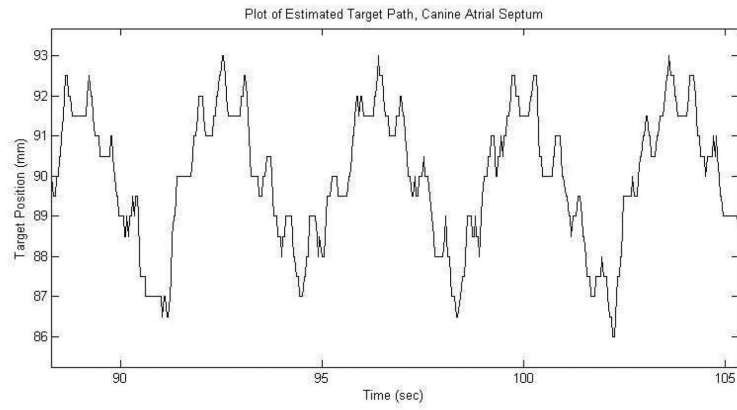motion tracking with motion (square), and no motion tracking with motion (circle).

Figure 9.
Plot of the estimated axial position of the target on the canine atrial septum during treatment.
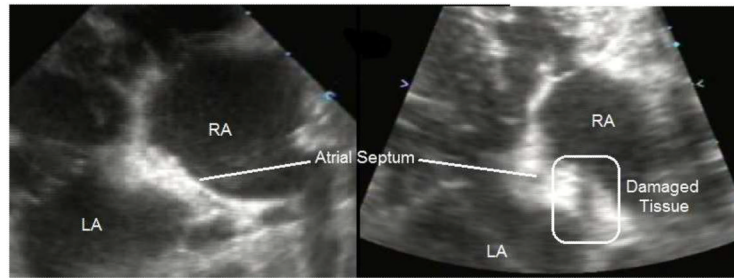
Figure 10.
Ultrasound images of the atrial septum before therapy (left), and after therapy (right) showing significantly reduced echogenicity across the treated region of the atrial septum, corresponding to regions of damaged or removed tissue.
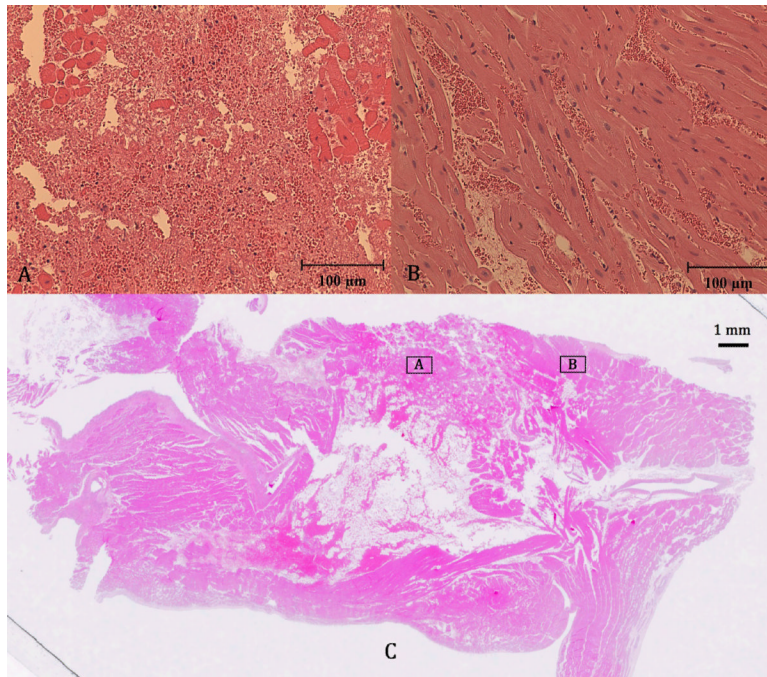
Figure 11.
Hematoxylin and Eosin (H&E) stained slide of treated atrial septum (C) along with close-up images of the fractionated region (A) and surrounding untreated region (B).

TABLE 1: RMS and Maximum Error versus Velocity

Maximum Velocity (mm/s)	Error (mm)	
	RMS	Maximum
10	0.25	0.65
20	0.31	1.05
30	0.41	1.74
40	0.51	1.75
50	0.58	2.18
60	0.63	2.04
70	0.64	2.26
80	0.66	2.96